Topology optimisation via the moving iso-surface threshold method: implementation and application

S. Vasista
srinivas.vasista@sydney.edu.au
L. Tong
liyong.tong@sydney.edu.au
School of Aerospace, Mechanical and Mechatronic Engineering
University of Sydney
Sydney, NSW
Australia

ABSTRACT

Topology optimisation is a useful tool for the design of aircraft structures. This work details how the new moving iso-surface threshold (MIST) topology optimisation method works and how it can be applied to aircraft structural design. This method has been coupled with commercial finite element analysis software in a simple manner without requiring the modification of the commercial software source code. In this way the user is able to take advantage of the finite element analysis tools such as automatic mesh generation and efficient solving. The extension of the method to 3D designs is also presented. The topology results of a 2D leading-edge rib for stiffness, stress and morphing objectives and a 3D wing skin stringer for stress design demonstrate the functionality of this method.

NOMENCLATURE

$\hat{a}, a$	filtered and original value of entity in the individual weight spatial filter
A	area of element
A_s	area of rod element representing spring
A_{tot}	total area of the finite element mesh

Paper No. 3937. Manuscript received 17 December 2012, accepted 21 November 2013.

https://doi.org/10.1017/S0001924000009143 Published online by Cambridge University Press

A^+, A^-	projected positive and negative areas in an element due to the intersection of Φ and S
E_s	elastic modulus of rod element representing spring
E_{solid}, E_{void}	solid and void elastic modulus material constants
f	constraining material fraction
$\mathbf{F}$	finite element load vector
g_r, g_s	general optimisation constraint functions
$\hat{H}, \hat{W}$	convolution operators for filtering
J	general structural optimisation objective function
k_s	spring stiffness
$\mathbf{k}$	element stiffness matrix
${}^b\mathbf{k}$	baseline element stiffness matrix
$\mathbf{K}$	global finite element analysis stiffness matrix
L_s	length of rod element representing spring
m	move limit on the element weighting factors
$\mathbf{n}$	unit outward normal of polyhedral face
N_E	total number of elements in the finite element mesh
N_F	total number of polyhedral faces of positive volume due to the intersection of Φ and S
N_P	number of elements within the filter radius
N_Q	number of nodes within the filter radius
N_V	number of vertices on a given element due to the intersection of Φ and S
$\mathbf{r}$	position vector of the centroid of polyhedral face
R_{ip}	distance between centroids of elements i and p
R_{jq}	distance between nodes j and q
R_{min}	filter radius
S	iso-surface
t	threshold level of iso-surface S
t_{min}, t_{max}	minimum and maximum bounds of threshold level during the bisection method material update routine
$\mathbf{u}$	element displacement vector
$\mathbf{U}$	global finite element analysis displacement vector
V^+	positive volume due to the intersection of Φ and S for 3D optimisation
W	work done by applied loads
x, $\mathbf{x}$	individual element weighting factor and vector of element weighting factors
${}_{new}x$	updated element weighting factor
X, Y, Z	general Cartesian co-ordinates
$\tilde{X}, \tilde{Y}$	co-ordinates of vertices formed due to the intersection of Φ and S
Φ	physical response function
α	angle-of-attack

https://doi.org/10.1017/S0001924000009143 Published online by Cambridge University Press

β	penalisation factor on element weighting factor
Γ	area of polyhedral face
Δx	maximum change in element weighting factors between optimisation iterations
$\Delta\hat{x}$	change in design as a fraction of total mesh area
$\varepsilon_x, \varepsilon_y, \gamma_{xy}$	2D components of strain
ζ	bisection method tolerance on material constraint
η	edge iso-point interpolation factor
$\sigma_x, \sigma_y, \tau_{xy}$	components of stress
σ_{vm}	von Mises stress

Subscripts

1, 2	end nodes of element edge
h	current polyhedral face
i	current element
j	current node
k	current iteration in the bisection method in the design update routine
l, *u*	lower and upper bounds on design variable
LC	current load case
p	current element within the filter radius
q	current node within the filter radius
s	sample number of iterations for optimisation convergence criteria
v	current vertex

Superscripts

(1)	input load case results
(2)	output load case results

1.0 INTRODUCTION

Topology optimisation methods have been used to design aircraft structures which have been proven to improve aircraft performance. Aircraft performance can be improved by, for example, saving weight, maximising structural stiffness and using morphing structures. In commercial aircraft, topology optimisation was used for the stiffness design of the inboard inner and outer fixed leading edge ribs and fuselage door intercostals of the Airbus A380 aircraft[1,2]. These applications of topology optimisation are believed to have led to weight savings of 1,000kg per A380 aircraft resulting in reduced fuel burn. In light of such weight advantages, attempts have been made to redesign the A380 main wing box[1] and the nacelle hinge bracket of the Airbus A320 aircraft[3]. Other examples of topology optimisation for the stiffness design of aircraft include the design of engine pylons[4] and a component of the vertical fin[5]. As there is a multitude of works on the use of topology optimisation for the design of morphing aircraft structures, detail is omitted from this paper and the reader is referred to review papers on morphing technology for more information on the influence of topology optimisation in morphing structural design[6-8].

There are a number of well-known topology optimisation methods in literature. The evolutionary structural optimisation (ESO)[9] uses a physical response function such as von Mises

https://doi.org/10.1017/S0001924000009143 Published online by Cambridge University Press

stress to gradually remove regions of low stress in a heuristic manner without using any explicit sensitivity analysis and mathematical programming methods. In the homogenisation method[10], an anisotropic composite with micro-scale voids is used to represent the material and for a given design case the optimal design is found by optimising these microstructures and their orientations. The solid isotropic material with penalisation (SIMP) based method[11-14] was introduced where the material properties are represented by one design variable per element with a penalisation factor. The topology optimisation problem using this SIMP based approach can be solved in a deterministic manner using gradient based mathematical programming methods such as optimality criteria (OC) and the method of moving asymptotes (MMA)[15] which require the calculation of the design variable sensitivities. The level set method[16-18] uses the zero level set of a higher-order surface function to implicitly define the structural boundary and the material properties are defined using an Ersatz material model[19]. The reader is referred to Refs 20-22 for a review and comparison on these methods.

The moving iso-surface threshold (MIST)[23] method is a recently formulated topology optimisation method which incorporates key features of the different above mentioned established topology optimisation methods. As a result, MIST offers some key advantages and the implementation is relatively simple. It has been demonstrated for a range of structural designs that MIST can generate optimal topologies without requiring sensitivity analysis[23,24]. As such, element stiffness matrices need not be stored/extracted and this lends itself to easier coupling with commercial finite element software without any modification to the commercial software source code. In this way users have complete control of and can continue research and development into the MIST method, as well as being able to exploit the powerful tools and functionality of the commercial software such as automatic mesh generation and efficient solving. This may be particularly useful in aircraft design where the design domain geometries tend to be more complex and, in future work, may lead to a more feasible aero-structural coupled optimisation framework.

The emphasis of this paper is the implementation of MIST and demonstration of the method in aircraft structures examples; for details on the proof-of-optimality and theoretical basis of the method the reader is referred to Ref. 23. Details on how MIST works are provided first followed by how MIST is coupled with an example commercial finite element analysis software (ANSYS® APDL 'Classic'[25]). Considerations and details of a mesh-independent filtering scheme and the extension to three-dimensional design cases are then presented. The functionality of MIST is then demonstrated for a number of two and three-dimensional aircraft design cases with different structural objectives. The routines in MIST were conducted using MATLAB®[26].

2.0 MIST ALGORITHM

MIST is a method used to solve topology optimisation problems such as that shown in Equation (1). The method aims to find the design variable values $\mathbf{x}$ and t (i.e. the material distribution) to minimise a certain structural objective function J, such as the total strain energy, subject to governing finite element equations g_r and material constraints g_s. As an overview of the MIST method, a physical response function Φ (stresses, strains and their appropriate combinations) is evaluated at all nodal points across the finite element design domain. The appropriate Φ function is chosen based on the structural objective and this function gives an indication of the relative structural performance of all points in the domain. An iso-surface S intersects the Φ function as shown in Fig. 1 and the contour formed by the intersection becomes the structural boundary. The level or threshold value t of the iso-surface S depends on the constraint. Weighting factors are used on the elements to represent the material distribution: void and solid elements are represented

https://doi.org/10.1017/S0001924000009143 Published online by Cambridge University Press

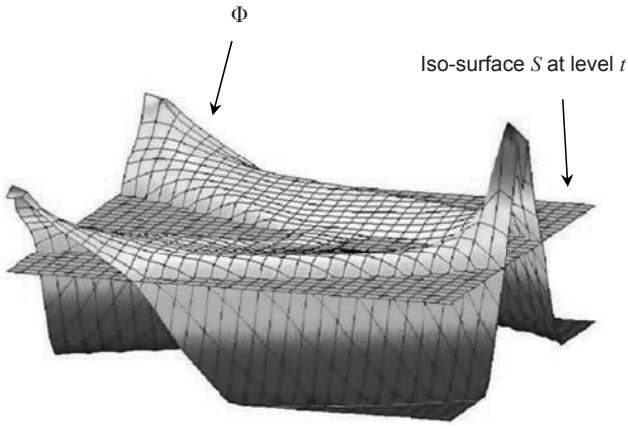


Figure 1. Schematics of response surface Φ and the intersection with the iso-surface.

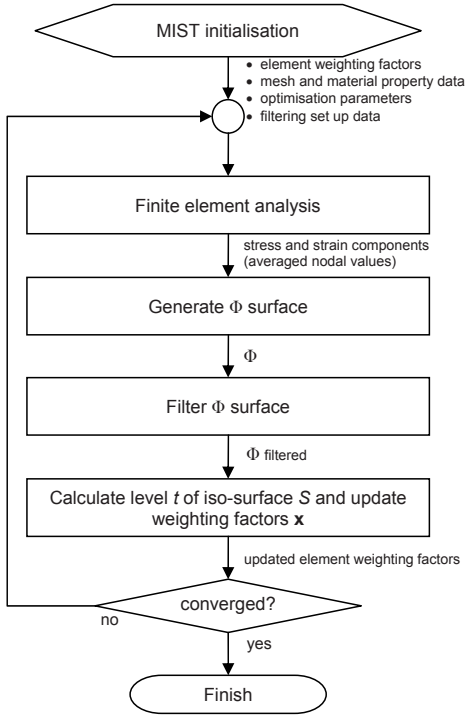


Figure 2. Flowchart of the MIST topology optimisation method.

by weighting factors of 0 and 1 respectively. In the element weighting factor update routine, the elements with Φ above the iso-surface at all nodes are assigned as or move towards solid material, and those elements with Φ below the iso-surface at all nodes are assigned as or move towards void material. For those elements with Φ values both above and below the iso-surface, the weighting factor is the fraction of the projected area above the iso-surface. The process flowchart is presented

https://doi.org/10.1017/S0001924000009143 Published online by Cambridge University Press

in Fig. 2 and the remainder of this section details the individual routines.

$$\begin{aligned} &\text{min: } J(\mathbf{x},t) \\ &\text{s.t.: } g_r(\mathbf{x},t) = 0 \\ &\quad g_s(\mathbf{x},\mathrm{t}) \le 0 \\ &\quad \mathbf{x}_l \le \mathbf{x} \le \mathbf{x}_u \end{aligned} \quad \ldots (1)$$

2.1 MIST initialisation

The finite element mesh is generated first in the MIST initialisation process. The nodal coordinate data table, element connectivity table and vector of element areas/volumes based on this mesh are stored. The constraint on the amount of material f is set. One weighting factor x_i is used per finite element (akin to element density design variables in SIMP gradient based methods). If there are non-design regions (i.e. regions which are specified to be either solid or void), then the weighting factors for the elements corresponding to the non-design regions are set to either 1 for solid or 0 for void. All remaining design region weighting factors are initialised uniformly with an intermediate value such that the material constraint is satisfied and all element weighting factors are stored in vector $\mathbf{x}$. Values for the material property model data are set: E_{solid}, E_{void} and penalisation factor β. Other optimisation parameters such as the stabilisation move limit and filter radius are also specified and the data for filtering is also set up in the MIST initialisation stage.

2.2 Finite element analysis

The material property for each element is calculated based on the corresponding weighting factor and using an appropriate material model such as the SIMP material model in Equation (2). These material properties are then assigned to the corresponding elements, boundary conditions and loads are applied, and the finite element analysis problem is solved. The objective function is calculated and component nodal stresses and strains (σ_x, σ_y, τ_{xy}, ε_x, ε_y, γ_{xy} for 2D cases for example) are calculated and stored. These nodal values are calculated by averaging the contribution from the elements attached to the given node.

$$E(x_i) = x_i^{\beta}(E_{solid} - E_{void}) + E_{void} \quad \ldots (2)$$

2.3 Generate and filter Φ surface

The generation of the Φ surface depends on the structural objective and these equations are summarised in Table 1. The surface for 2D analysis is formed by plotting Φ values as Z co-ordinates at the X and Y locations of the corresponding nodes.

For mesh independency reasons, the Φ function is filtered. This filtering scheme is explained in Section 4.0.

Table 1
Summary of Φ calculation for different structural objectives (2D)

Objective	Choice for Φ	How Φ is calculated at node j
min: total strain energy	strain energy density	$\Phi_j = \frac{1}{2}(\sigma_{x_j}\varepsilon_{x_j} + \sigma_{y_j}\varepsilon_{y_j} + \tau_{xy_j}\gamma_{xy_j})$
min: max von Mises stress	von Mises stress	$\Phi_j = \sigma_{\mathrm{vm}_j}$
max: displacement	mutual strain energy density	$\Phi_j = -(\sigma_{x_j}^{(2)}\varepsilon_{x_j}^{(1)} + \sigma_{y_j}^{(2)}\varepsilon_{y_j}^{(1)} + \tau_{xy_j}^{(2)}\gamma_{xy_j}^{(1)})$

https://doi.org/10.1017/S0001924000009143 Published online by Cambridge University Press

2.4 Calculate level *t* of iso-surface *S* and update weighting factors x

The iso-surface level t is calculated using an iterative bisection method and the element weighting factors are updated. The level t is calculated such that the material constraint is met. In this method, the initial value for t is the average of the minimum and maximum of Φ. The difference between Φ and t is calculated at all points in the design domain, all design region element weighting factors are updated where i is the current element and N_E is the total number of elements in the mesh,

and the amount of material is summed $\sum_{i=1}^{N_E}\left(x_{i_k} A_i\right)$ where A_i is the area of element i and k is

the current iteration in the bisection method. If this summed material is greater than the material constraint fA_{tot} (where A_{tot} is the total mesh area), t_{min} is updated as the current value t_k and the iso-surface moves up for the next iteration. If the summed material is less than the material constraint, t_{max} is updated as the current value t_k and the iso-surface moves down to the new level for the next iteration. This process is repeated until the summed material is within a small tolerance ζ (e.g. 1×10^{-4}) of the material constraint. If there are non-design solid and/or void regions present, the value of $\Phi - t_k$ is set to a positive number (e.g. 0·01) at all nodes on the non-design solid elements and a negative number (e.g. −0·01) at all nodes on the non-design void elements for every bisection iteration k. The steps in this process are given as follows:

Step 1: Determine $t_{max0} = max(\Phi)$ and $t_{min0} = min(\Phi)$ for a known Φ

Step 2: Calculate iso-surface level: $t_k = \dfrac{t_{\max_k} + t_{\min_k}}{2}$

Step 3: Calculate $\Phi - t_k$ at all nodes, set $\Phi - t_k$ to 0·01 and −0·01 at solid and void non-design nodes respectively and update x_{ik} for all elements based on area ratio

Step 4: If $\left|\dfrac{\sum_{i=1}^{N_E}\left(x_{i_k} A_i\right)}{fA_{tot}} - 1\right| < \zeta$, terminate iteration; otherwise

Case (a) $\left.\begin{array}{l} t_{\min_{k+1}} = t_k \\ t_{\max_{k+1}} = t_{\max_k} \end{array}\right\}$ if $\sum_{i=1}^{N_E}\left(x_{i_k} A_i\right) > A_{tot}$

or

Case (b) $\left.\begin{array}{l} t_{\min_{k+1}} = t_{\min_k} \\ t_{\max_{k+1}} = t_k \end{array}\right\}$ if $\sum_{i=1}^{N_E}\left(x_{i_k} A_i\right) > A_{tot}$

then go to Step 2 and repeat

For Step 3, x_{ik} is calculated for each element based on the values of $\Phi - t_k$ at the element nodes. If $\Phi - t_k$ is positive at all element nodes, x_{ik} moves towards 1. If $\Phi - t_k$ is negative at all element nodes, then x_{ik} moves towards 0. If the value of $\Phi - tk$ is positive at some node(s) and negative at other(s), then x_{ik} is based on the ratio of projected positive area to total element area as shown in Fig. 3 and Equation (3).

https://doi.org/10.1017/S0001924000009143 Published online by Cambridge University Press

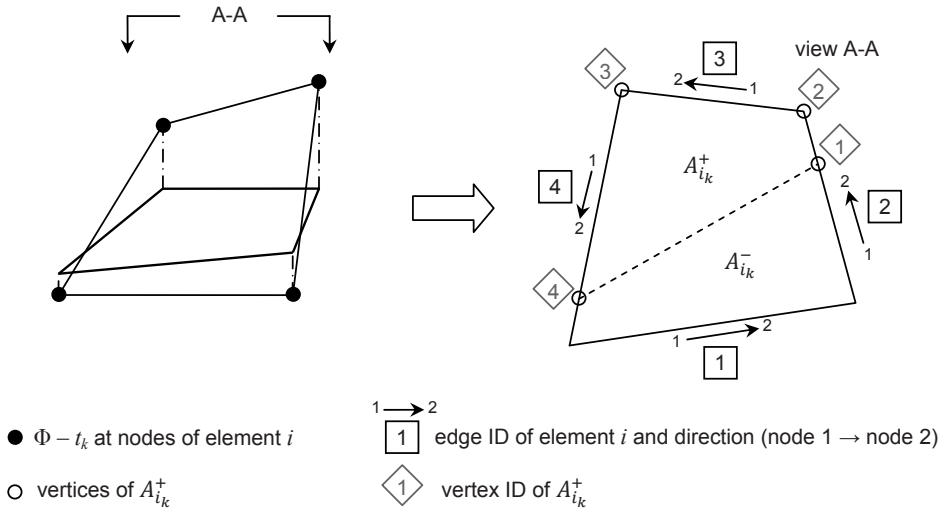


Figure 3. 3D view of nodal values of $\Phi - t_k$ for element i and the corresponding top view showing projected positive and negative areas.

$$x_{i_k} = \frac{A^+_{i_k}}{A^+_{i_k} + A^-_{i_k}} = \frac{A^+_{i_k}}{A_i} \qquad \ldots (3)$$

The value of the positive projected area $A^+_{i_k}$ is determined by calculating the coordinates of the vertices of $A^+_{i_k}$ via an edge-based process and uses the element connectivity table data. To describe this process, consider Fig. 3 as an example scenario. The process starts on edge 1 of the element and identifies that the values of $\Phi - t_k$ at the end nodes of the edge are both negative. Therefore there is no vertex of $A^+_{i_k}$ on edge 1. Moving to edge 2, node 1 (which was node 2 of edge 1) is negative and node 2 is positive: therefore vertex 1 lies on edge 2. The X and Y co-ordinates of vertex 1 are calculated by interpolating the X and Y co-ordinates of the end nodes of edge 2 based on the ratio of the magnitudes of $\Phi - t_k$ at the end nodes of edge 2. This is given in Equation 4 where the subscripts 1 and 2 refer to the end nodes of the edge and subscript v and tilde accent refer to the vertex co-ordinates. As node 2 of edge 2 is positive, this is vertex 2. On edge 3, both end nodes are positive. As node 1 on edge 3 was node 2 of edge 2 and vertex 2 is already defined, node 2 of edge 3 is vertex 3. On edge 4, node 1 is positive and node 2 is negative, therefore the last vertex lies on this edge. The co-ordinates of vertex 4 are calculated using Equation (4) again.

$$\eta = \frac{\left|\Phi - t_k\right|_1}{\left|\Phi - t_k\right|_1 + \left|\Phi - t_k\right|_2} \qquad \ldots (4(a))$$

$$\tilde{X}_v = X_1 + \eta(X_2 - X_1) \qquad \ldots (4(b))$$

$$\tilde{Y}_v = Y_1 + \eta(Y_2 - Y_1) \qquad \ldots (4(c))$$

Once the co-ordinates of all vertices of $A^+_{i_k}$ are determined, the area $A^+_{i_k}$ is determined using the standard method for determining the area of a non-self-intersecting (simple) arbitrary polygon using vertex co-ordinate data[29]:

https://doi.org/10.1017/S0001924000009143 Published online by Cambridge University Press

$$A_{i_k}^{+} = \frac{1}{2}\sum_{v=1}^{N_V}\left(\tilde{X}_v\tilde{Y}_{v+1} - \tilde{X}_{v+1}\tilde{Y}_v\right) \quad \ldots (5)$$

where N_V is the number of vertices of $A_{i_k}^{+}$ and $\tilde{X}_{N_V+1}$ and $\tilde{Y}_{N_V+1}$ are equal to $\tilde{X}_1$ and $\tilde{Y}_1$ respectively to 'close' the polygon.

A move limit m on the weighting factors can be used to restrict large variations between optimisation iterations to stabilise the MIST solution. This can be implemented in a simple manner in this routine where Equation (3) is replaced with:

$$X_{i_k} = \begin{cases} \frac{A_{ik}^{+}}{A_i} & \text{if } \left|\frac{A_{ik}^{+}}{A_i} - x_{i_o}\right| \le m \\ x_{i_o} + \text{sign}\left(\frac{A_{ik}^{+}}{A_i} - x_{i_o}\right)m & \text{if } \left|\frac{A_{ik}^{+}}{A_i} - x_{i_o}\right| > m \end{cases} \quad \ldots (6)$$

where x_{i0} is the value of the element weighting factor before any bisections were made (i.e. the current value of element weighting factor in the main optimisation loop).

With this, the change in weighting factors between optimisation iterations is restricted. As such, the element weighting factors no longer change from solid to void but rather the value of $\Phi - t_k$ determines in which direction the weighting factors 'move' towards: i.e. if the values of $\Phi - t_k$ are positive for all element nodes then the element weighting factor moves towards solid and if the values of $\Phi - tk$ are negative for all element nodes then the element weighting factor moves towards void. In this manner, the element weighting factors take intermediate values (i.e. between 0 and 1) in the early iterations of the optimisation process. When the optimisation process has converged and terminated, the plot of weighting factors and the plot of the contour of the intersection between Φ and S correlate and the solution is that of a binary 0-1 solid-void representation.

When the summed material has converged to a value within the specified tolerance as given in Step 4 of this routine, the resultant element weighting factors are used for the next iteration in the main optimisation loop as shown in Equation 7.

$$\text{new}^x i = x_{i_k} \quad \ldots (7)$$

2.5 Convergence criteria

Following standard topology optimisation procedures, the optimisation process can be said to be converged when the change in each element weighting factor is less than a certain percentage as given in Equation (8a). In MIST, this criterion may be too strict in some cases leading to the optimiser running without termination even though the objective function and overall topology are unchanging. This convergence criteria can be relaxed to consider the change of element weighting factors as a fraction of the total design domain as shown in Equation (8b) and/or by how much the element weighting factors have moved (as a fraction of the total design domain) over a sample set of iterations as shown in Equation (8c). In Equation (8c), the left subscript s is the sample number of iterations which is an even number such as 6 and is defined by the user.

$$^{a}\Delta x = \max\left(\left|_{new}\mathbf{x} - \mathbf{x}\right|\right) \quad \ldots (8(a))$$

$$^{b}\Delta x = \frac{\sum_{i=1}^{N_E}\left(\left|_{new}x_i - x_i\right|A_i\right)}{\sum_{i=1}^{N_E}A_i} = \frac{\sum_{i=1}^{N_E}\left(\left|_{new}x_i - x_i\right|A_i\right)}{A_{tot}} \quad \ldots (8(b))$$

$$^{c}\Delta x = \frac{\sum_{i=1}^{N_E}\left(\left|_{new}x_i - _{new-s}x_i\right|A_i\right)}{\sum_{i=1}^{N_E}A_i} = \frac{\sum_{i=1}^{N_E}\left(\left|_{new}x_i - _{new-s}x_i\right|A_i\right)}{A_{tot}} \quad \ldots (8(c))$$

https://doi.org/10.1017/S0001924000009143 Published online by Cambridge University Press

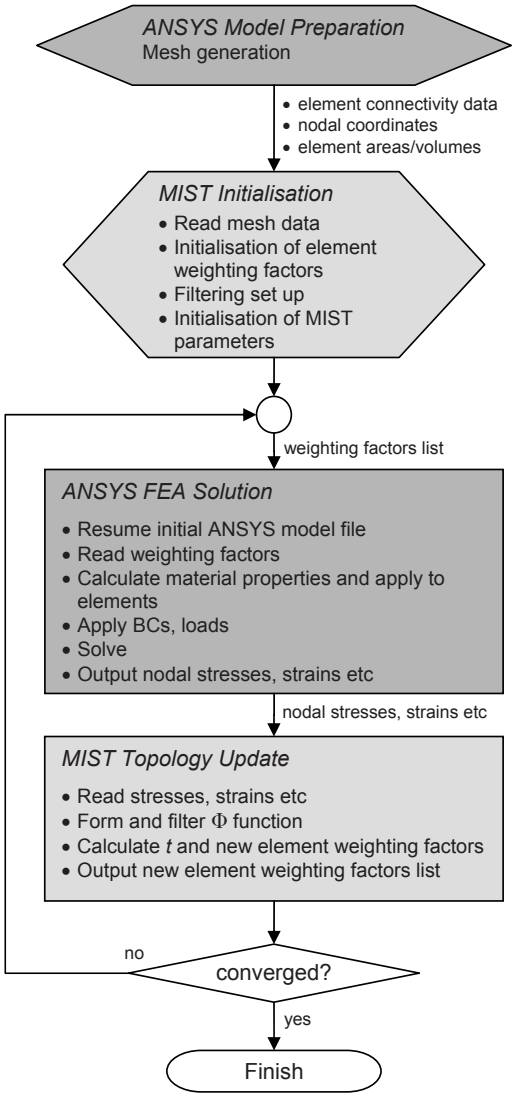


Figure 4. Flowchart of MIST with coupling with commercial finite element analysis software.

3.0 COUPLING WITH COMMERCIAL FINITE ELEMENT ANALYSIS SOFTWARE

The finite element routine in the MIST method can be conducted using commercial finite element software without the need to modify the commercial software source code. As mentioned, optimal solutions can be achieved in MIST without conducting sensitivity analysis and only the physical responses need to be reported. This makes the MIST method relatively more feasible to couple with commercial software as the physical responses of nodal stresses and strains are often readily available for output as opposed to the element stiffness matrices. Essentially, the finite element analysis routine is treated as a 'black-box' where the input is the list of element weighting factors

https://doi.org/10.1017/S0001924000009143 Published online by Cambridge University Press

and the output is the stress and strain data. However, it should be noted that the commercial software needs to be able to read and write data in an automated manner. The interface between MIST and ANSYS is conducted in a simple manner where this input and output data is stored as text data files which are read and written at each optimisation iteration. The architecture of the coupling is presented in Fig. 4.

A finite element model is generated in ANSYS first. The mesh and real constants (plate thicknesses, section properties, etc) are created and the element connectivity table, nodal coordinates table and list of element areas (or volumes for 3D optimisation) are exported. The ANSYS model file is saved for calling at a later stage in the optimisation process. The mesh data is then read into the MIST program in MATLAB and the optimisation parameters such as the mass limit, penalisation etc are initialised and the vector of initial weighting factors is exported as a text file. The filtering distances for the convolution operators are also calculated in the MIST initialisation stage. The optimisation loop now begins and ANSYS is run in an automated fashion in a simple one-line-of-code manner by using the shell escape operator '!' in MATLAB. In this line of code, the ANSYS program executable file is run in batch mode with an associated ANSYS input file written by the user. In this input file: (*i*) the previously saved initial ANSYS model file is resumed and saved as a new file (to preserve the initial model file); (*ii*) the list of element weighting factors are read; (*iii*) the material properties are calculated according to the material model in Equation (2) and assigned to the corresponding elements (where it should be noted that there is one material property per element); (*iv*) the loads and boundary conditions are applied; (*v*) the model is solved; and (*vi*) the desired nodal stress, strain, etc values are exported as text files. The algorithm returns to MATLAB where MIST then reads these physical responses and then continues with the remainder of the loop as described in the previous section: Φ is formed and filtered, the correct threshold level t is calculated and the element weighting factors are updated. These new weighting factors are saved in a text file to be read by ANSYS in the next optimisation iteration. This process repeats until the design has converged. It should also be noted that ANSYS always resumes the initial model file thereby reducing computational time by not having to generate the same mesh every iteration. Furthermore, the ANSYS input file does not require modification during the process.

A number of examples of MIST topology optimisation using ANSYS as the finite element analysis sub-routine for the design of aircraft structures are presented in Section 6.0.

4.0 FILTERING SCHEMES IN MIST

As structural responses may change as the finite element mesh changes (i.e. refining the mesh), the Φ function may change and the resultant topology may be dependent on the mesh. Mesh dependency problems are common to topology optimisation and have been investigated previously. The reader is referred to Ref. 28 for an overview of mesh dependency problems and proposed methods for overcoming them.

One way of overcoming the mesh dependency problem for gradient-based topology optimisation is to filter the element sensitivities as proposed by Sigmund[29]. This method is purely heuristic though it produces results similar to the local gradient constrained method[28]. In this method, the sensitivity of a specific element is modified based on a weighted average of the element sensitivities within a fixed spatial neighbourhood (radius). This is shown in Fig. 5(a) and Equation (9)

where $\frac{\partial \hat{f}}{\partial x}$ and $\frac{\partial f}{\partial x}$ are the modified and original element sensitivities respectively, i is the specified element, N_p is the number of elements within the spatial radius R_{min}, p is the current element in

https://doi.org/10.1017/S0001924000009143 Published online by Cambridge University Press

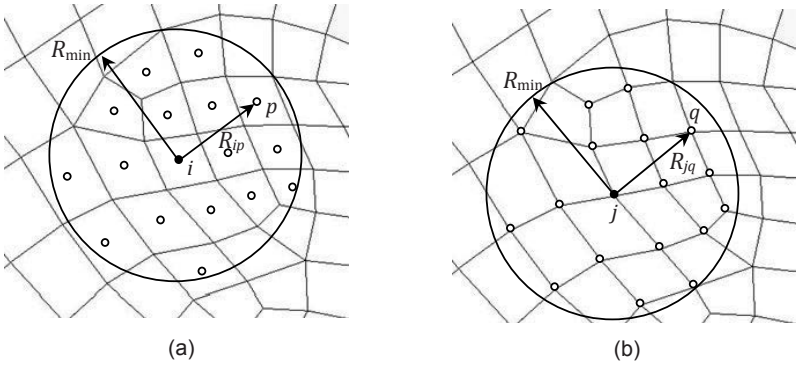


Figure 5. Schematics of filtering of (a) element based values (e.g. weighting factors, densities, sensitivities) and (b) nodal based Φ values.

the spatial region and $\hat{H}_p$ is the convolution operator. $\hat{H}_p$ is defined as $\tilde{R_{min}} - R_{ip}$ where R_{ip} is the distance between the centroids of elements i and p. The convolution operator is zero outside the filter region and for element p decays linearly with the distance from the element i.

$$\frac{\hat{\partial f}}{\partial x_i} = (x_i)^{-1} \frac{\sum_{p=1}^{N_P} \hat{H}_p x_p \frac{\partial f}{\partial x_p}}{\sum_{p=1}^{N_P} \hat{H}_p} \quad \ldots (9)$$

The weighting factors in MIST can be filtered in a similar heuristic approach where the weighting factor of a given element x_i is modified based on the linear weighted average of weighting factors of elements within a spatial neighbourhood. An alternative to the filter in Equation (9) is the individual weight spatial filter (IWSF) proposed by Cardoso and Fonseca[30] as shown in Equation (10). This filter can be used on a number of fields, such as element weighting factors in MIST, and densities or sensitivities in gradient based methods. In this equation, $\hat{a}$ and a are the modified and original values of element weighting factors, A is element area and $\hat{W}_p$ is the convolution operator defined as $1 - \frac{R_{ip}}{R_{min}}$. This filter takes into consideration the size of the elements within the filtering region and thus can be used with any mesh with arbitrarily shaped elements.

Calculating the centroid-to-centroid distances and determining the elements within the radial neighbourhood for each optimisation iteration is computationally expensive. In order to reduce this computational expense, the centroid distances and identification of the neighbouring elements can be performed once in the initialisation routine as the mesh does not change over the iterations. The convolution operator $\hat{W}_p$ is precalculated and stored using a variable data size storage scheme such as a cell array in MATLAB, where the cell index refers to the given element i, and the cell contents of this index is a vector of the normalised convoluted distances $1 - \frac{R_{ip}}{R_{min}}$ from the centroid of element i to the centroids of neighbouring elements p.

$$\hat{a}_i - \frac{a_i A_i + \sum_{p=1}^{N_P} \hat{W}_p a_p A_p}{A_i + \sum_{p=1}^{N_P} \hat{W}_p A_p} \quad \ldots (10)$$

To investigate the effects of this filter, a typical maximum stiffness design case of a MBB beam (600 × 100mm) is used with three mesh strategies: (1) a rectangular mesh of 2,400 elements

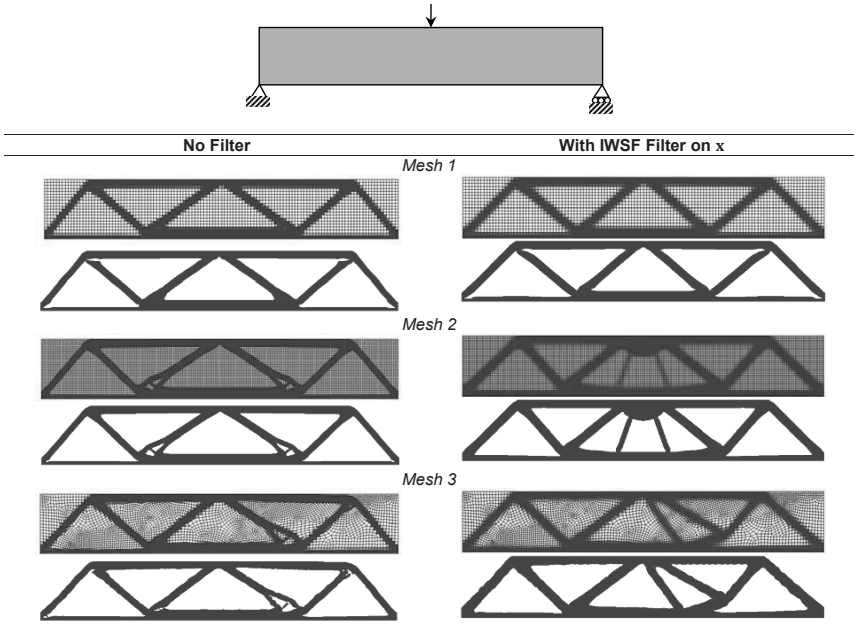
https://doi.org/10.1017/S0001924000009143 Published online by Cambridge University Press

(element size 5mm); (2) a finer rectangular mesh of 9,600 elements (element size 2·5mm); and (3) a mesh with 2,400 arbitrarily shaped elements (including Tri3 and Quad4 elements). Results are presented without the use of a filter and with a filter size of 7·5mm (R_{min}). The SIMP material model scheme was used with a penalty exponent of 3, solid elastic modulus E_{solid} of 70GPa, void elastic modulus E_{void} of 0·001, Poisson's ratio v of 0·3 and plate thickness of 50mm. A material fraction of 0·35 and a move limit of 0·1 were used and a force of 1kN was placed at the midpoint of the top edge.

It is clear from the first column of Table 2 that the topology varies with different finite element meshes when no filtering scheme is used. However, it should be noted that the topologies do not have checkerboards and only differ in the localised regions where the truss-like members connect rather than over the entire the design domain such as that in Fig. 1(d) in Ref. 28. This is due to the 'pre-filtering' effect caused when using the averaged nodal stress and strain components for generating Φ. The results in the second column of Table 2 show that this filtering scheme reduces the complexity of the structure at the joints of the truss-like members. However, the topologies vary for the different meshes and thus does not overcome the mesh-dependency problem for MIST.

An investigation into filtering the Φ surface was conducted as an alternative to filtering the element weighting factors. The Φ value at a specific node is modified based on the linear weighted average of Φ values at nodes within a spatial neighbourhood. As Φ is calculated at nodal locations, the centre of the spatial filter for a specific node is the nodal location and node-to-node distances of neighbouring nodes are computed rather than the element centroid-to-centroid distances. This

Table 2
MBB maximum stiffness design case and resultant topologies without any filtering and with filtering on element weighting factors. Top figures are element weighting factors, bottom figures are the contours formed due to the intersection of Φ and *S*



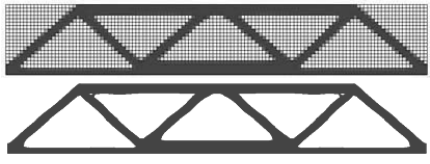
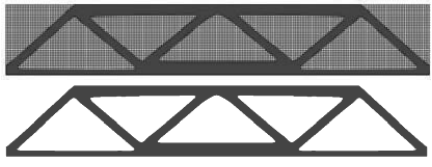
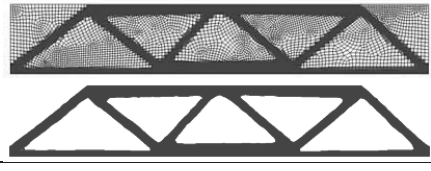
https://doi.org/10.1017/S0001924000009143 Published online by Cambridge University Press

is shown in Fig. 5(b) and Equation (11) where $\hat{\Phi}$ and Φ are the modified and original values respectively, j is the specified node, and N_Q and q are the number of nodes and the current node in the spatial region respectively. $\hat{W}_q$ is the convolution operator defined as $1-\frac{R_{jq}}{R_{min}}$ where R_{jq} is the distance between nodes j and q. Furthermore, the value of the element weighting factor x_i and the size of element i are not considered as the Φ values are based at nodal points only. Similar to the case of filtering element weighting factors, the node-to-node distances and identification of the neighbouring nodes can be performed once in the initialisation routine where the convolution operator $\hat{W}_q$ is precalculated and stored in order to reduce the computational expense.

$$\hat{\Phi}_j = \frac{\sum_{q=1}^{N_Q} \hat{W}_q \Phi_q}{\sum_{q=1}^{N_Q} \hat{W}_q} \quad \ldots (11)$$

The above MBB example was re-run in MIST using the filtering scheme on Φ to determine if this scheme led to mesh independent designs. The results in Table 3 show that the Φ filtering scheme is a viable solution to the mesh dependency problem in MIST as evident with the topologies being near-identical for different meshes when a filter is used. It should be noted that additional filters can be used and further investigation is possible. Increasing the radius of the filter may be required for mesh-independency as the effects of further-field connectivity would be considered. Increasing the filter radius may also lead to structures with less topological complexities and this suggests that the filter radius needs to be chosen appropriately. Given the results here, the filtering scheme used here was also used in the subsequent examples in this paper.

Table 3
Results of filtering Φ

With Φ Filter
Mesh 1

Mesh 2

Mesh 3


https://doi.org/10.1017/S0001924000009143 Published online by Cambridge University Press

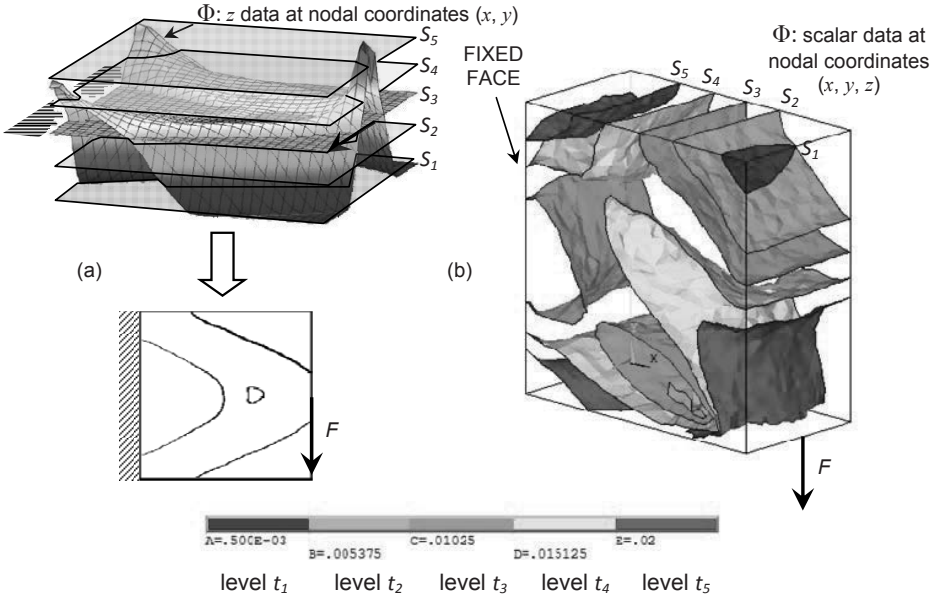


Figure 6. Comparison of Φ, *S* and *t* for 2D and 3D cases. (a) 2D cantilever beam optimisation: (top) Φ and *S* at levels t_1 to t_5; (bottom) topological contour formed due to the intersection of Φ and isosurface S_3. (b) 3D cantilever beam optimisation: iso-surfaces at the different threshold levels.

5.0 EXTENSION TO 3D STRUCTURES

The theoretical formulation of 3D optimisation is the same as the 2D case with the addition of the *Z*-displacement degree of freedom. Conceptually, the functioning of MIST is slightly different for 3D cases and requires the consideration of volumes rather than areas. As with the 2D case, the iso-surface connects points in the design domain which have the same Φ value. However, it is now a complex 3D surface as opposed to a horizontal plane for the 2D case as shown in Fig. 6. The threshold value can be visualised as moving inward or outward normal to the iso-surface instead of moving vertically up or down. Again, the bisection method as described in Section 2.5 is used to find the threshold value *t* of such that the volume enclosed by the iso-surface (and the capped ends of the design domain) satisfies the material constraint. The weighting factor moves towards 1 for those elements with $\Phi - t_k$ greater than zero at all nodes, and the weighting factor moves towards 0 for those elements with $\Phi - t_k$ less than zero at all nodes. For those elements with $\Phi - t_k$ values both larger and smaller than zero at different nodes, the weighting factor is based on the volume ratio as shown in Fig. 7 and defined in Equation (12).

$$X_{i_k} - \frac{V_{i_k}^{+}}{V_i} \qquad \ldots (12)$$

The iso-surfaces are calculated using an edge-based method. The program finds the co-ordinates of the iso-points (if they exist) along the element edges and forms faces on the iso-surface and capped element ends from these isopoints and nodal points. The volume of the positive solid region $V_{i_k}^{+}$ is then calculated via the divergence theorem as used for calculating the volume of an arbitrary polyhedral as given in Equation 13[31], where **P** = 1/3 **r**, **r** is the position vector of the centroid of the current face *h*, Γ is the area of the face, **n** is the unit normal of *h* pointing outwards, and N_F is the total number of faces of the enclosed volume formed by the iso-points and nodal points.

https://doi.org/10.1017/S0001924000009143 Published online by Cambridge University Press

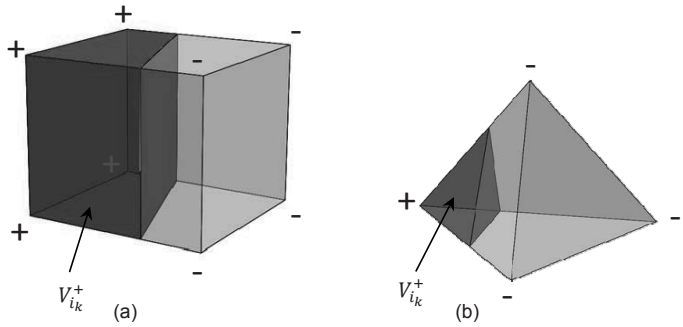


Figure 7. Schematic of volume ratio calculation based on nodal $\Phi - t_\kappa$ values for (a) hexahedral and (b) tetrahedral elements.

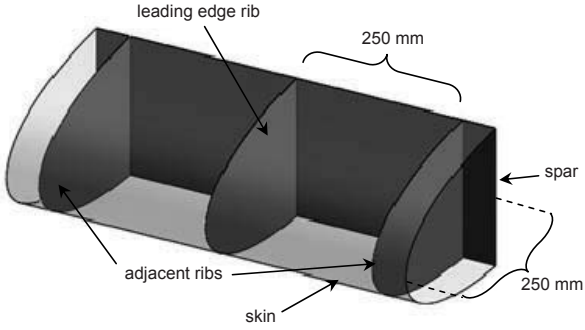


Figure 8. Example of a wing leading-edge structural assembly.

$$V_{i_k}^+ = \int_\Omega \operatorname{div} \mathbf{P}\, \mathrm{d}\Omega = \oint \mathbf{P} \cdot \mathbf{n}\, \mathrm{d}\Gamma$$
$$V_{i_k}^+ = \tfrac{1}{3} \sum_{h=1}^{N_F} \mathbf{r}_h \cdot \mathbf{n}_h \Gamma_h \qquad \ldots (13)$$

Filtering the Φ function can also be conducted for 3D cases where the Φ values at nodes within a spherical spatial neighbourhood with radius R_{min} are used to modify the Φ value at the specified central node.

6.0 EXAMPLES

6.1 2D wing leading edge rib

The first case study considered was optimisation of a two-dimensional leading edge wing rib. The rib topology was optimised for three sub-cases separately: maximum stiffness, fully stressed and compliant morphing designs. A general typical structural assembly shown in Fig. 8 features multiple ribs, a wing skin and spar and this single wing leading edge rib was optimised in isolation from the surrounding components. The wing was assumed to be of constant section (i.e. untapered) with a uniform rib spacing of 250mm. The profile for the leading edge rib was the first quarter-chord

https://doi.org/10.1017/S0001924000009143 Published online by Cambridge University Press

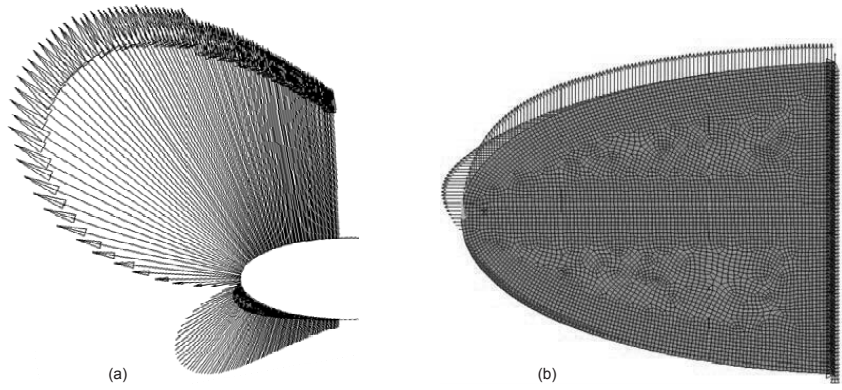


Figure 9. (a) XFOIL aerodynamic loading and (b) equivalent finite element analysis nodal loads.

(250mm) of a NACA0021 aerofoil with a chord length of 1,000mm. The load case for stiffness and stress designs was the aerodynamic loading of this wing at 10° angle-of-attack and 100ms^{-1} (194kt) velocity at sea level, representative of a jet-powered UAV. The leading edge rib was isolated from the other wing components by using some idealisations of the boundary conditions and loads: a cantilever restraint on the edge attached to the spar was used and the appropriate aerodynamic loads from the skin were transferred onto the rib. It was assumed that the rib was attached to the skin continuously along the rib edge and that the aerodynamic load was assumed to be transmitted from the skin to the ribs equally across the span. In this way the pressure distribution was first accumulated across 250mm in the spanwise direction (125mm both inboard and outboard of the rib) and then applied onto the rib edge. These boundary conditions and loads are appropriate for these demonstration purposes of MIST. For final designs in future work, the optimisation process should consider analysis of the complete structural assembly in order to capture effects such as the load transfer from one component to another. This may be possible via superelement/substructuring techniques in which case MIST can still readily be used as the topology optimisation tool.

The aerodynamic distribution (pressure coefficients) was computed using the viscid formulation in XFOIL[32]. The parameters used in XFOIL were a Reynolds number of 1×10^7, angle-of-attack of 10°, and velocity of 100ms^{-1} and the resultant pressure distribution is shown in Fig. 9(a). The list of pressure coefficients calculated at points along the leading edge was exported from XFOIL as a text file. From this the X and Y components of these pressure coefficients were calculated and then transferred into values of pressure by multiplying them by dynamic pressure where the air density used was 1·225kg/m^3. These pressures were then converted to nodal forces by multiplying the accumulated span length (250mm) and using standard load vector assemblage finite element procedures. The resultant horizontal and vertical forces were –314N and 1,039N respectively. It should be noted that (1) the location of the points used in the XFOIL aerofoil model coincided with the nodal locations in the finite element analysis for ease of load data transfer and (2) the aerodynamic loads were not updated during the optimisation process.

The ANSYS structural model is shown in Fig. 9(b). The mesh consisted of 6,473 four-node quadrilateral PLANE182 plane stress elements with 1mm thickness and a linear static analysis was used. While the overall geometry of the leading-edge rib was symmetric, the mesh was generated using the in-built automeshing tools in ANSYS and was not symmetric. The SIMP material model in Equation 2 was used with values representing aluminium (E_{solid} = 70GPa, E_{void} = 0·001, Poisson's ratio of 0·3).

https://doi.org/10.1017/S0001924000009143 Published online by Cambridge University Press

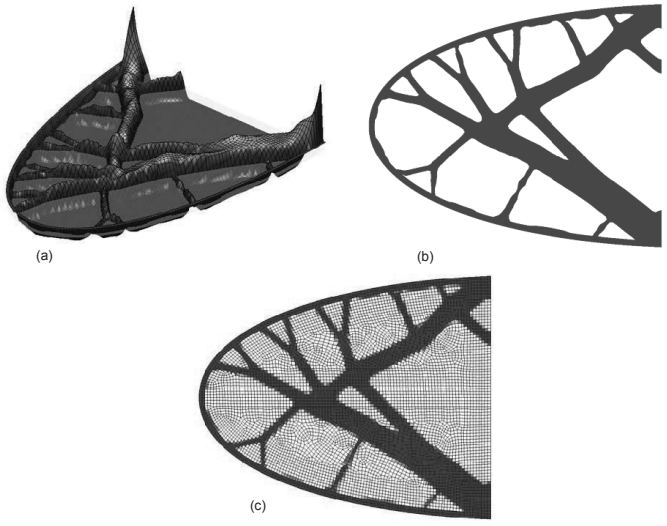


Figure 10. Schematics of (a) intersection of Φ and *S*, (b) resultant contour topology and (c) element weighting factors for the single load case maximum stiffness design.

A solid non-design region was applied to the elements on the leading edge. A material fraction of 0·35 was used for all optimisation sub-cases and the initial value of the design region weighting factors were set to a uniform intermediate value such that the total material $\sum_{i=1}^{N_E}(x_i A_i)$ was equal to the material constraint fA_{tot}. A penalisation factor β of 3 was applied to the weighting factors, and a move limit on the weighting factors of 0·1 and a filter on Φ with radius of 5mm were used.

6.1.1 Maximum stiffness design

The overall equivalent stiffness of the rib was maximised by minimising the total strain energy in the design domain whilst subject to a mass constraint as given in Equation (14). The Φ function used was the strain energy density computed at the finite element nodes. The three-components of averaged stress and strain (σ_x, σ_y, τ_{xy}, ε_x, ε_y, γ_{xy}) at the nodal points were output by ANSYS and then multiplied and added together according to Equation (15), where *j* is the current node, in the Φ function calculation subroutine in MIST.

$$\begin{aligned} &\min : \tfrac{1}{2}\int_{\Omega} \boldsymbol{\sigma}^T \varepsilon d\Omega \\ &s.t. : \mathbf{KU} = \mathbf{F} \\ &\frac{\sum_{i=1}^{N_E}(x_i A_i)}{A_{tot}} \le f \\ &0 \le \mathbf{x} \le 1 \end{aligned} \qquad \ldots (14)$$

$$\Phi_j = \tfrac{1}{2}\left(\sigma_{xj}\varepsilon_{xj} + \sigma_{yj}\varepsilon_{yj} + \tau_{xy}\gamma_{xy_j}\right) \qquad \ldots (15)$$

Figure 10(a) shows the plot of Φ and its intersection with *S* after the final optimisation iteration. The contour formed from this intersection is shown in Fig. 10(b) from which corresponding weighting factors, shown in Fig. 10(c), are computed and input into the finite element analysis routine. Fig.

https://doi.org/10.1017/S0001924000009143 Published online by Cambridge University Press

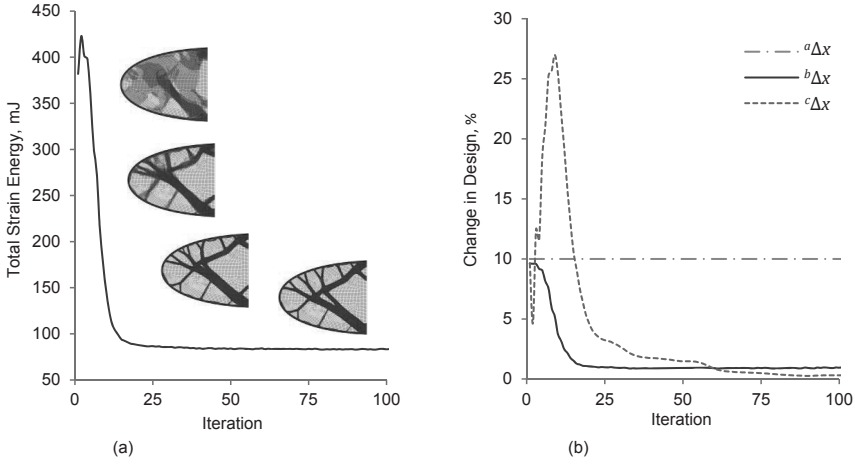


Figure 11. Histories of (a) total strain energy (objective function) and (b) change in design for the maximum stiffness design case.

10(b) can be considered as the final topology for manufacturing considerations as the plots of Fig. 10(b) and (c) correlate. The topology result features 'branch' like structural members and resembles that of typical structures optimised for a distributed load such as the bridge example in Ref. 33. It is clear that more material is distributed to the upper portion of the aerofoil as the loading is higher on the upper skin. The objective function history in Fig. 11(a) shows smooth convergence from an initial value of 382mJ to 83mJ, a reduction of 78% and the maximum displacement of the final solution was 0·057mm at the foremost point of the leading edge. Figure 11(b) shows that the maximum absolute change in element weighting factors (criterion $^{a}\Delta x$ in Equation (8a)) is 10% throughout the optimisation process, corresponding to the move limit of 0·1. As this value does not decrease, $^{a}\Delta x$ cannot be used as the termination criteria and hence $^{b}\Delta x$ or $^{c}\Delta x$ should be used as indicated by the final values within 1%.

To compare the functionality of MIST, this maximum stiffness design case was also solved using the SIMP material model in conjunction with the gradient based MMA. The problem statement was to minimise the work done by the aerodynamic load (i.e. half of the mean compliance) as given in Equation (16). This gradient-based optimisation case could not be coupled with ANSYS as element stiffness matrices cannot be exported from ANSYS. As such, the entire optimisation process was performed in MATLAB and the finite element analysis routine had to be coded, resulting in a significantly less streamlined process than that of MIST. Using the same mesh as the MIST case, the baseline element stiffness matrices $^{b}\mathbf{k}_i$ (i.e. with a unit elastic modulus and Poissons ratio of 0·3) for all elements were first calculated and stored. The actual element stiffness matrices $\mathbf{k}_i$ were calculated by using the SIMP material model for elastic modulus and multiplying this by the baseline matrices as shown in Equation (17). The global stiffness matrix was assembled in the finite element analysis routine and the finite element analysis equation was solved for displacements. The element sensitivities were calculated by multiplying the first derivative of the SIMP model (with respect to the design variable) with the baseline element stiffness matrices and element displacements as per the standard adjoint method. This is represented in Equation (17). The sensitivities were filtered using the individual weight spatial filter given in Equation (10) with a filter size of 5mm.

https://doi.org/10.1017/S0001924000009143 Published online by Cambridge University Press

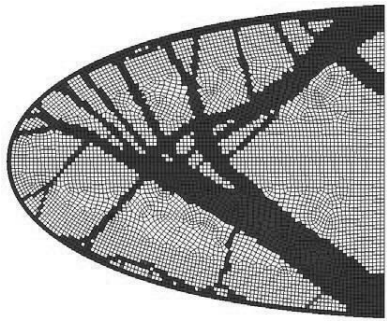


Figure 12. Resultant topology for the maximum stiffness design case using SIMP and gradient-based MMA.

$$\begin{gathered} \min: W(\mathbf{x}) \tfrac{1}{2} \mathbf{U}^T \mathbf{K} \mathbf{U} = \tfrac{1}{2} \sum_{i=1}^{N_E} \mathbf{u}_i{}^T \mathbf{k}_i(x_i) \mathbf{u}_i \\ s.t.: \mathbf{K}\mathbf{U} = \mathbf{F} \\ \frac{\sum_{i=1}^{N_E} (x_i A_i)}{A_{tot}} \le f \\ 0 \le \mathbf{x} \le 1 \end{gathered} \quad \ldots (16)$$

$$\mathbf{k}_i(x_i) = E(x_i)^b \mathbf{k}_i$$

$$\frac{\partial W}{\partial x_i} = -\frac{1}{2} \mathbf{u}_i{}^T \frac{\partial \mathbf{k}_i(x_i)}{\partial x_i} \mathbf{u}_i = -\frac{1}{2} \mathbf{u}_i{}^T \frac{\partial E(x_i)}{\partial x_i}{}^b \mathbf{k}_i \mathbf{u}_i = -\frac{1}{2} \mathbf{u}_i{}^T \beta x_i^{\beta-1} \left(E_{solid} - E_{void}\right)^b \mathbf{k}_i \mathbf{u}_i \quad \ldots (17)$$

The SIMP – MMA result in Fig. 12 largely resembles that of the MIST solution. Two large diagonal trusses start from the top and bottom corners of the right edge and connect in the central region of the rib. A short 'strut' connects the upper diagonal truss to the right edge and smaller 'branches' connect the upper diagonal truss to the upper skin. Again, more material is distributed to the upper region as the aerodynamic load is larger on the upper skin. The final value of the work done by the aerodynamic load in Fig. 13 is 77mJ, lower than but comparable to the 83mJ of total stored strain energy in the MIST case. The smooth history of convergence criteria ${}^b\Delta x$ and ${}^c\Delta x$ and their final values within 1% demonstrate that these should be used for the termination of the optimisation process. These similarities in final topology and objective function values between the MIST and SIMP – MMA solutions demonstrate the functionality of the MIST method.

6.1.2 Fully stressed design

In this subcase, MIST was used with the aim of designing a leading edge structure with a stress distribution as uniform as possible. The problem is stated as the minimisation of the maximum von Mises stress as shown in Equation (18). The averaged nodal von Mises stress was used to define Φ and the optimisation parameters were the same as the maximum stiffness design case.

A certain set of nodes was excluded when determining the maximum von Mises stress. These were: (1) nodes in non-design regions; (2) nodes attached to non-solid elements (i.e. elements whose weighting factors were not (1) because the values of stress for intermediate-valued weighting factors are not representative of the actual material response; and (3) restrained nodes directly on the right edge in order to exclude the contribution of highly localised stress singularities. As such, only design region nodes, solid element nodes and free nodes were considered in the objective function. The issue of stress singularities may be addressed by using the extended finite element method (XFEM) similar to Ref. 18 or other mesh enrichment techniques which may lead to improved designs.

https://doi.org/10.1017/S0001924000009143 Published online by Cambridge University Press

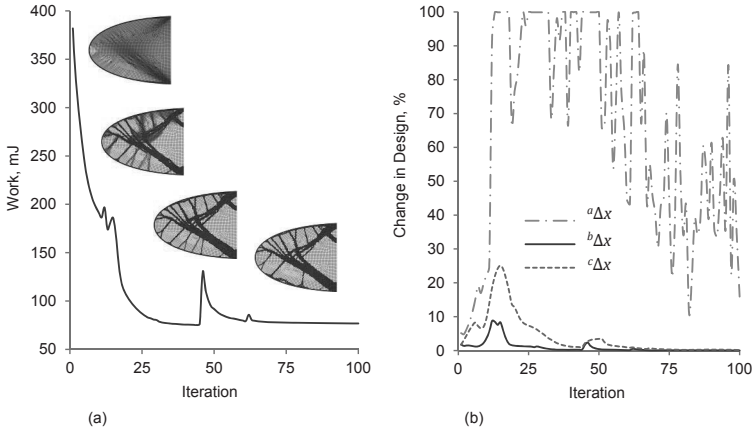


Figure 13. Histories of (a) work done by the aerodynamic load and (b) change in design for the maximum stiffness design case solved using SIMP and the gradient-based MMA method.

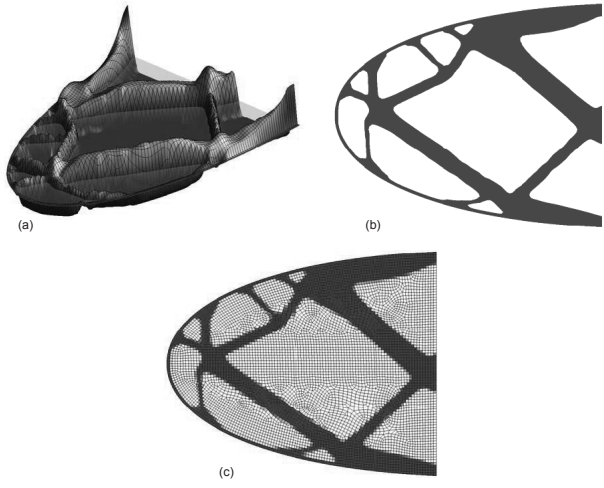


Figure 14. Schematics of (a) intersection of Φ and S, (b) resultant contour topology and (c) element weighting factors for the fully stressed design case.

$$\begin{aligned} &\min : \max \sigma_{VM} \\ &s.t. : \mathbf{KU} = \mathbf{F} \\ &\frac{\sum_{i=1}^{N_E} (x_i A_i)}{A_{tot}} \le f \\ &0 \le \mathbf{x} \le 1 \end{aligned} \qquad \ldots (18)$$

Figures 14(b) and (c) depict the resultant topology obtained from the intersection of Φ and the iso-surface S shown in Fig. 14(a) and these plots of topology, element weighting factors and intersection all correlate. Figure 15 shows the history of the maximum and minimum von Mises stress in the design domain and the stress ratio (minimum divided by maximum). The graph shows

https://doi.org/10.1017/S0001924000009143 Published online by Cambridge University Press

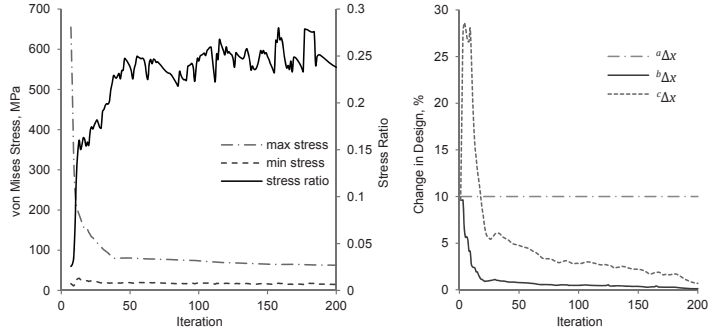


Figure 15. Histories of von Mises stress including minimum to maximum stress ratio and change in design for the fully stressed design case.

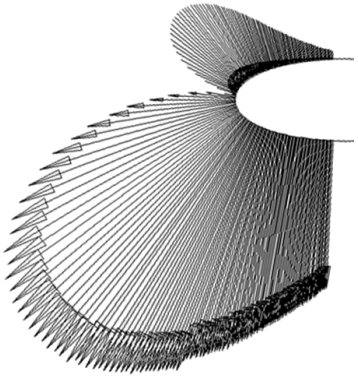


Figure 16. Aerodynamic loading for an angle-of-attack of –10°.

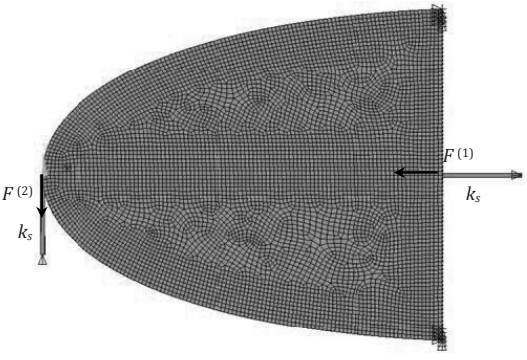


Figure 17. Finite element model for morphing droop nose with rod elements used as input and output springs.

a decreasing maximum von Mises stress as per the objective function and an increasing ratio of minimum to maximum von Mises stress. The final values are a maximum stress of 65MPa and stress ratio of 0·26. Also, the final change in design is within 1%.

6.1.3 Multiple load cases

The previous topologies show optimal designs for a single loading condition. These designs may not be suitable for different loading scenarios. In order to account for load variations, multiple load cases are considered in the formation of Φ. In the following examples, the previous aerodynamic pressure distribution is reversed as an additional load case, corresponding to the aircraft in a nose-down orientation of –10° at the same velocity and atmospheric conditions as shown in Fig. 16. The Φ function is now an aggregate of the Φ function of the two individual load cases as shown in Equation 19. In this manner the combined Φ function is an equally weighted sum of the Φ responses for the individual load cases.

$$\Phi = \sum_{LC=1}^{N_{LC}} \Phi_{LC} \qquad \ldots (19)$$

https://doi.org/10.1017/S0001924000009143 Published online by Cambridge University Press

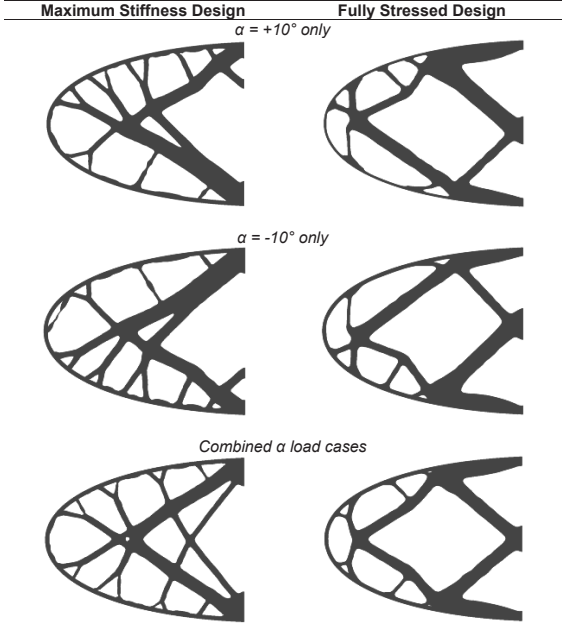
The results of the multiple load case are shown in Table 4 and compared with the designs optimised for the +10° and –10° angles of attack individually. As expected, the topologies for the –10° are near-mirror images of the +10° design cases. Also, the multiple load case results are almost symmetric and show that the structure is capable of efficiently supporting the range aerodynamic loads encountered between these angle of attack limits. It should be mentioned that these minor differences in the symmetry of the topologies may be alleviated by increasing the Φ filter radius.

6.1.4 Compliant mechanism design

In this example, the design of a compliant mechanism-based morphing droop-nose wing was investigated. MIST was used to solve the compliant mechanism problem, stated as maximising the displacement at a given output port as shown in Equation 20. A simple single-input-single-output case was considered for this droop-nose problem, where the input actuation force was placed at the midpoint of the right edge in the $-X$ direction, and the objective was to maximise the output displacement at the foremost point on the leading edge in the $-Y$ direction as shown in Fig. 17. The mutual strain energy density was used as Φ and was calculated in component form as shown in Equation (21). This required the results of the solutions of two load cases: (1) the strain from the input load case and (2) the stress from output load case where a unit dummy force was applied at the output port and in the desired direction.

The geometry and mesh were the same as the previous leading edge examples and the elements on the edge were non-design solid elements to represent the skin. The nodes at the top right and bottom right regions were fixed in X and Y displacements. Non-dimensional units were used with E_{solid} and E_{void} values of 1 and 0·001 respectively. The penalisation factor and move limit

Table 4
Comparison of topologies for single load cases of +10° and –10° angles-of-attack and topology for the multiple load case combination of +10° and –10° angles-of-attack



https://doi.org/10.1017/S0001924000009143 Published online by Cambridge University Press

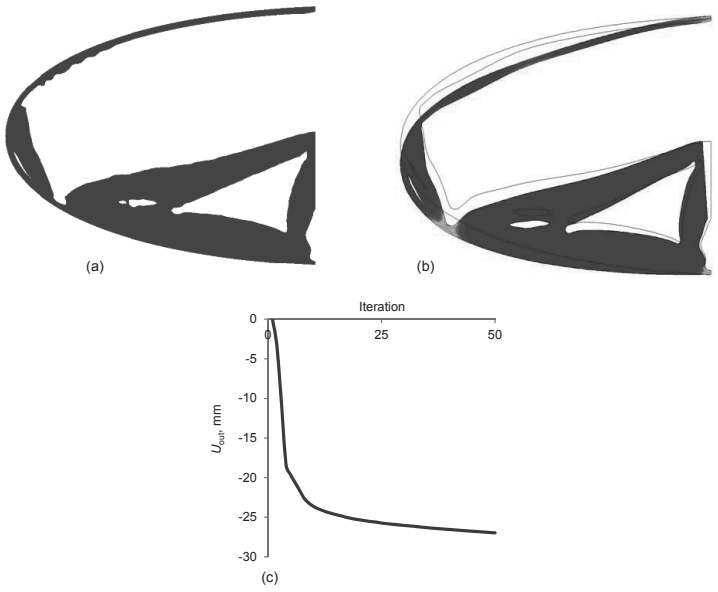


Figure 18. Leading edge droop-nose case (a) resultant topology; (b) finite element analysis showing displaced configuration with von Mises stresses overlaid on undeformed configuration; and (c) objective function history where the upward *Y* direction is defined as positive.

were 3 and 0·1 respectively. The solution of the compliant mechanism required input and output springs and these were modelled using rod elements (LINK180) in ANSYS as shown in Fig. 17. The stiffness of the springs could be adjusted by modifying either the spring elastic modulus E_s, length L_s or cross-sectional area A_s as given by spring stiffness relation in Equation (22). For this example, the elastic modulus, length and cross-sectional area of the springs were 0·1, 50 and 5 respectively resulting in a spring stiffness of 0·01. The magnitudes of the input and output forces were 1 each. The aerodynamic load distribution was not applied, rather the springs were used as a means of resistance against which the compliant mechanism output work.

$$\begin{gathered} \max: u_{out} = \min: -u_{out} = -\int_{\Omega} \boldsymbol{\sigma}^{(2)^T} \boldsymbol{\varepsilon}^{(1)} d\Omega \\ s.t.: \mathbf{KU} = \mathbf{F} \\ \frac{\sum_{i=1}^{N_E} (x_i A_i)}{A_{tot}} \le f \\ 0 \le \mathbf{x} \le 1 \end{gathered} \quad \ldots (20)$$

$$\Phi_j = -\left(\sigma_{x_j}^{(2)} \varepsilon_{x_j}^{(1)} + \sigma_{y_j}^{(2)} \varepsilon_{y_j}^{(1)} + \tau_{xy_j}^{(2)} \gamma_{xy_j}^{(1)} \right) \quad \ldots (21)$$

$$k_s = \frac{E_s A_s}{L_s} \quad \ldots (22)$$

Figure 18(a) shows that in the resultant topology material is distributed in the lower half of the design domain, connecting the input and output ports. Finite element analysis on this resultant topology was conducted and the result in Fig. 18(b) shows that the compliant mechanism converts the input actuation into downward deflection at the leading edge tip. This is largely due to the pivoting

https://doi.org/10.1017/S0001924000009143 Published online by Cambridge University Press

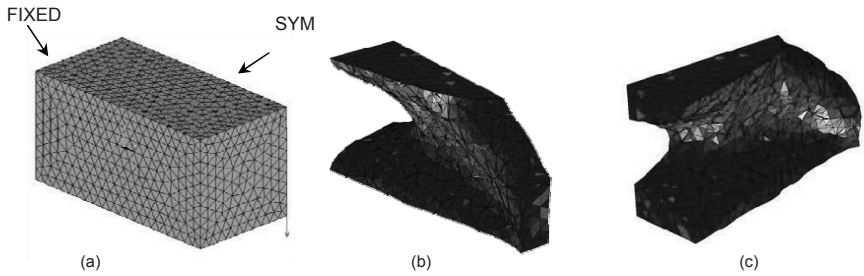


Figure 19 (a) Finite element model for the 3D cantilever beam optimisation case. (b) Topology result and (c) reverse view of result.

motion at the bottom right nodes and hinge point in the lower part of the compliant mechanism. Figure 18(c) shows that the objective function has been achieved with smooth convergence to a final displacement of –27mm.

However, other issues need to be first addressed for the successful design of the morphing wing concept. Of primary importance is the need to consider multiple output points and not just a single point as the overall profile of the leading edge is crucial to the aerodynamic efficiency. An extension to the MIST method is required to include a shape control formulation where the objective could be to minimise the least squares error between a set of actuated and target displacements at selected points. Concentrated stresses, such as those shown in Fig. 18(b), need to be prevented and this may be addressed by using stress constraints and by using pressurised fluid as a means of distributed actuation. Aerodynamic loads and how they change during the morphing process need to be accounted for through an aero-structural coupled analysis and large structural displacements require non-linear finite element analysis. Other aspects requiring consideration include the introduction of input energy constraints or including the magnitude of the actuation force as an additional design variable. All these considerations require a reformulation of the morphing wing design problem.

Whilst additional aspects need consideration for a successful morphing design, this example shows that the problem of maximising displacement can be achieved with MIST and that the selection of mutual strain energy density as Φ yields appropriate results. This example also shows that compliant mechanism problems can be solved when coupled with commercial finite element analysis software by using rod elements to represent input and output springs. Benchmark examples in Refs 23 and 24 further show MIST as a method capable of solving compliant mechanism problems.

6.2 3D structures

6.2.1 Cantilever beam

A benchmark test case of a cantilever beam is presented first. Non-dimensional units were used and the design domain was a rectangular volume of $2 \times 1 \times 0{\cdot}5$ units. This volume was meshed with 15,356 four-node tetrahedral (SOLID185) elements as shown in Fig. 19(a). Symmetric boundary conditions were applied on the rear face and the left face was fully fixed. A unit load was applied at the tip and the von Mises stress was used as Φ for a fully stressed design case. The result shown in Figs 19(b) and (c) is representative of a typical cantilever topology optimisation result and demonstrates the functionality of the 3D MIST optimisation method.

https://doi.org/10.1017/S0001924000009143 Published online by Cambridge University Press

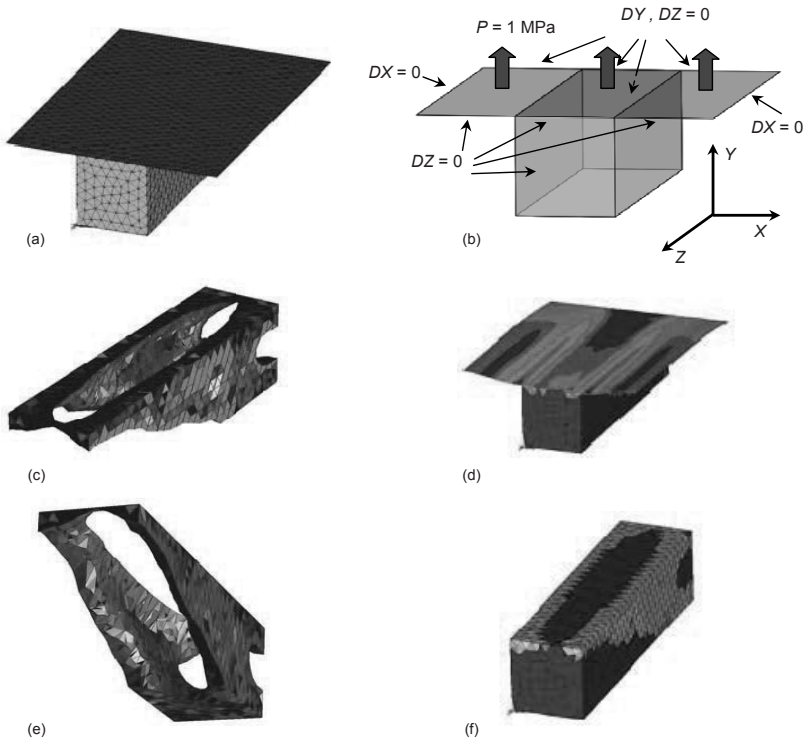


Figure 20. Schematics of the wing skin stringer example: (a) boundary conditions and loading; (b) finite element model; (c) and (e) different orientations of the topology result; (d) and (e) finite element analysis results showing von Mises stresses of the skin-stringer assembly and stringer in isolation respectively.

6.2.2 Wing stringer

An aircraft wing stringer was optimised for a fully stressed design. This example illustrates how commercial finite element analysis software can be used to efficiently generate a model with multiple element types and then be optimised. The finite element model as shown in Fig. 20(a) includes plate elements to represent the skin and to enforce appropriate load transfer from the aerodynamic pressure load (assumed to be uniform) to the stringer. The stringer volume dimensioned 200 × 50 × 50mm and the skin overhang was 50mm on either side of the stringer. The skin thickness was 2mm and was offset such that the bottom face of the skin was flush with the top face of the stringer. The solid and plate elements had common nodes at their interface thus ensuring proper mesh compatibility. Periodic boundary conditions were used on the relevant plate edges and solid faces as shown in Fig. 20(b). The material used was aluminium for both stringer and skin with a Young's Modulus of 70GPa and Poisson's ratio of 0·3. A penalisation factor of 3 and move limit of 0·1 were used.

Figures 20(c) and (e) show different orientations of the topology result. The converged shape bears resemblance to a half span of an arch bridge, indicating a feasible result. The deformed skin in Fig. 20(d) shows low deformation and high stress (in the skin) at points attached to the stringer whilst the stringer itself has a relatively homogeneous stress distribution as shown in Fig. 20(f).

https://doi.org/10.1017/S0001924000009143 Published online by Cambridge University Press

7.0 CONCLUSION

This paper demonstrates the functionality of the new MIST topology optimisation method and presents an efficient way of coupling the optimisation process with commercial finite element analysis software. In doing this, the user has access to the powerful tools of the commercial software whilst still having full control of the optimisation process.

The MIST method was extended to include 3D optimisation and several 2D and 3D wing structure examples were presented using this coupled method. The stiffness and stress designs were intuitive and had some features representative of typical structures designed for stiffness and stress objectives. For future work, considerations of the effects of load transfer from one component to another can be achieved via the use of superelement and substructuring techniques. The morphing design cases proved to be functional from an optimisation perspective. However, a shape control formulation amongst other considerations need to be developed in MIST which will result in a more robust design method leading to more feasible and practical morphing designs.

ACKNOWLEDGEMENTS

Srinivas Vasista is a recipient of the Australian Postgraduate Award and the R.W. McKenzie Scholarship for Aeronautical Sciences and Technology and is grateful for the support from the Commonwealth Government of Australia and the R.W. McKenzie Centre. The authors would like to thank the support of the Australian Research Council (Grant No. DP110104123) and Prof. Krister Svanberg for providing the method of moving asymptotes MATLAB codes.

REFERENCES

1. KROG, L., TUCKER, A., KEMP M. and BOYD, R. Topology optimization of aircraft wing box ribs, 2004, Altair Technology Conference.
2. KROG, L., TUCKER, A. and ROLLEMA, G. Application of topology, sizing and shape optimization methods to optimal design of aircraft components, 2002, Altair Engineering, pp 11-1 - 11-11, UK.
3. TOMLIN, M. and MEYER, J. Topology optimization of an additive layer manufactured (ALM) aerospace part, Seventh Altair CAE Technology Conference, 2011.
4. REMOUCHAMPS, A., BRUYNEEL, M., FLEURY, C. and GRIHON, S. Application of a bi-level scheme including topology optimization to the design of an aircraft pylon, *Structural and Multidisciplinary Optimization*, 2011, **44**, (6), pp 739-750.
5. SALEEM, W., YUQING, F. and YUNQIAO, W. Application of topology optimization and manufacturing simulations – a new trend in design of aircraft components, 2008, International Multiconference of Engineers and Computer Scientists, Hong Kong.
6. VASISTA, S., TONG, L. and WONG, K.C. Realization of morphing wings – a multidisciplinary challenge, *J Aircr*, 2012, **49**, (1), pp 11-28.
7. BARBARINO, S., BILGEN, O., AJAJ, R.M., FRISWELL, M.I. and INMAN, D.J. A review of morphing aircraft, *J Intelligent Material Systems and Structures*, 2011, **22**, (9), pp 823-877.
8. THILL, C., ETCHES, J., BOND, I., POTTER, K. and WEAVER, P. Morphing skins, *Aeronaut J*, 2008, **112**, (3), pp 117-138.
9. XIE, Y.M. and STEVEN, G.P. A simple evolutionary procedure for structural optimization, *Computers & Structures*, 1993, **49**, (5), pp 885-896.
10. BENDSØE, M.P. and KIKUCHI, N. Generating optimal topology in structural design using a homogenization method, *Computer Methods in Applied Mechanics and Engineering*, 1988, **71**, (1), pp 197-224.
11. BENDSØE, M.P. Optimal shape design as a material distribution problem, *Structural and Multidisciplinary Optimization*, 1989, **1**, (4), pp 193-202.
12. ZHOU, M. and ROZVANY, G.I.N. The COC algorithm, part II: Topological, geometrical and generalized shape optimization, *Computer Methods in Applied Mechanics and Engineering*, 1991, **89**, (1-3), pp 309-336.

https://doi.org/10.1017/S0001924000009143 Published online by Cambridge University Press

13. MLEJNEK, H.P. Some aspects of the genesis of structures, *Structural and Multidisciplinary Optimization*, 1992, **5**, (1), pp 64-69.
14. BENDSØE, M.P. and SIGMUND, O. Material interpolation schemes in topology optimization, *Archive of Applied Mechanics*, 1999, **69**, (9), pp 635-654.
15. SVANBERG, K. The method of moving asymptotes – a new method for structural optimization, *Int J for Numerical Methods in Engineering*, 1987, **24**, (2), pp 359-373.
16. SETHIAN, J.A. and WEIGMANN, A. Structural boundary design via level set and immersed interface methods, *J Computational Physics*, 2000, **163**, (2), pp 489-528.
17. WANG, M.Y., WANG, X.M. and GUO, D.M. A level set method for structural topology optimization, *Computer Methods in Applied Mechanics and Eng*, 2003, **192**, pp 227-246.
18. LUO, Z. and TONG, L. A level set method for shape and topology optimization of large displacement compliant mechanisms, *Int J for Numerical Methods in Eng*, 2008, **76**, (6), pp 862-892.
19. ALLAIRE, G., JOUVE, F. and TOADER, A.-M. Structural optimization using sensitivity analysis and a level-set method, *J Computational Physics*, 2004, **194**, (1), pp 363-393.
20. ROZVANY, G. A critical review of established methods of structural topology optimization, *Structural and Multidisciplinary Optimization*, 2009, **37**, (3), pp 217-237.
21. PATEL, N.M., TILLOTSON, D., RENAUD, J.E., TOVAR, A. and IZUI, K. Comparative study of topology optimization techniques, *AIAA J*, 2008, **46**, (8), pp 1963-1975.
22. ESCHENAUER, H.A. and OLHOFF, N. Topology optimization of continuum structures: A review, *Applied Mechanics Reviews*, 2001, **54**, (4), pp 331-390.
23. TONG, L. and LIN, J. Structural topology optimization with implicit design variable – optimality and algorithm, *Finite Elements in Analysis and Design*, 2011, **47**, (8), pp 922-932.
24. VASISTA, S. and TONG, L. Design and testing of pressurized cellular planar morphing structures, *AIAA J*, 2012, **50**, (6), pp 1328-1338.
25. ANSYS, ANSYS mechanical APDL structural analysis guide, Software Package, Version 13.0, 2010, ANSYS, Canonsburg, PA, USA.
26. The Mathworks Inc, Matlab, Software Package, Version R2012b, 2012, Natick, MA, USA.
27. ZWILLINGER, D. (ED). *CRC Standard Mathematical Tables and Formulae*, 2003, Chapman and Hall / CRC Press, Boca Raton, FL, USA.
28. SIGMUND, O. and PETERSSON, J. Numerical instabilities in topology optimization: A survey on procedures dealing with checkerboards, mesh-dependencies and local minima, *Structural Optimization*, 1998, **16**, (1), pp 68-75.
29. SIGMUND, O. On the design of compliant mechanisms using topology optimization, *Mechanics of Structures and Machines*, 1997, **25**, (4), pp 493-524.
30. CARDOSO, E.L. and FONSECA, J.S.O. Complexity control in the topology optimization of continuum structures, *J Brazilian Society of Mechanical Sciences and Engineering*, 2003, **25**, pp 293-301.
31. KREYZSIG, E. Triple integrals, Divergence theorem of gauss, *Advanced Engineering Mathematics*, Seventh edition, 1993, John Wiley and Sons, Singapore, pp 544-546.
32. DRELA, M. and YOUNGREN, H. XFOIL, Software Package, Version 6.9, 2001.
33. SIGMUND, O. and CLAUSEN, P.M. Topology optimization using a mixed formulation: An alternative way to solve pressure load problems, *Computer Methods in Applied Mechanics and Engineering*, 2007, **196**, (13-16), pp 1874-1889.

https://doi.org/10.1017/S0001924000009143 Published online by Cambridge University Press